The Astrophysical Journal, 649:1110–1123, 2006 October 1

THEORETICAL INVESTIGATION OF THE ONSETS OF TYPE II RADIO BURSTS DURING SOLAR ERUPTIONS

Jun Lin
National Astronomical Observatories of China/Yunnan Astronomical Observatory, Chinese Academy of Sciences, P.O. Box 110, Kunming, Yunnan 650011, China; and Harvard-Smithsonian Center for Astrophysics, 60 Garden Street, Cambridge, MA 02138

Salvatore Mancuso
INAF/Osservatorio Astronomico di Torino, 20 Strada Osservatorio, I-10025 Pino Torinese, Italy

and

Angelos Vourlidas
Solar Physics Branch, Naval Research Laboratory, 4555 Overlook Avenue, SW, Washington, DC 20375
Received 2006 February 14; accepted 2006 June 5

ABSTRACT

On the basis of previous works, we investigated coronal mass ejection (CME) propagations and the consequent type II radio bursts invoked by the CME-driven shocks. The results indicate that the onset of type II bursts depends on the local Alfvén speed (or the magnetoacoustic wave speed in the non–force-free environment), which is governed by both the magnetic field and the plasma density. This determines that the type II burst cannot appear at any altitude. Instead, its onset positions can never be lower than a critical height for the given coronal environment, which consequently determines the start frequencies of the emission: for an eruption taking place in the magnetic configuration with a background field of 100 G, the onset of type II bursts should occur at around 0.5 $R_\odot$ from the solar surface, and the corresponding start frequency of the fundamental component is about 150 MHz. This result is consistent with similar estimates based on observations that bring the corresponding frequency to a few hundred MHz. Our results further indicate that the onset of type II bursts depends on the rate of magnetic reconnection as well. When magnetic reconnection during the eruption is not fast enough, a type II burst may not occur at all even if the associated CME is fast (say, faster than 800 km s^{-1}). This may account for the fast and radio-quiet CMEs. Related to these results, properties of the associated solar flares and type III radio bursts, especially those used as the precursors of the type II radio bursts, are also discussed.

Subject headings: Sun: coronal mass ejections (CMEs) — Sun: flares — Sun: magnetic fields — Sun: radio radiation

Online material: color figure

1. INTRODUCTION

It is now generally accepted that a typical solar eruptive process manifests three different but related phenomena: solar flares, eruptive prominences, and coronal mass ejections (CMEs). In such a process, a huge amount of magnetized plasma and energy can be flowing into the outermost corona and interplanetary space at a considerably large speed, say, a few times 10^3 km s^{-1} (e.g., Forbes 2000; Klimchuk 2001; Priest & Forbes 2002; Lin et al. 2003). As the bulk of the magnetized plasma (the CME) propagates through the corona at high speed, it is very likely to invoke and to drive a fast-mode shock ahead of it like a piston when its velocity exceeds the local magnetoacoustic speed (or the Alfvén speed, in a force-free environment such as the solar corona). The long-duration gradual solar energetic particle events (see Lee 2005 for a review), the type II radio bursts observed during major eruptions (Cane et al. 2002; Vourlidas 2004; Gopalswamy 2004a, 2004b), and the broadening and the Doppler dimming shown by the spectral profiles of O VI and Lyα lines (Raymond et al. 2000; Mancuso et al. 2002) constitute convincing evidence of the passage and the propagation of the CME-driven shocks. A recent statistical study by Mancuso & Raymond (2004) further suggests that all type II radio bursts might be piston-driven, originating at the tops or flanks of CMEs.

An alternative exciter of the type II radio burst is the so-called blast wave, which is believed to originate in proximity to the solar flare. This scenario is obviously based on the idea that the flare takes place explosively, like a bomb blowing out the nearby material in every direction. Unlike the CME-driven shock, to our knowledge, there is not a rigorous theory describing the dynamical properties of the driver of such a wave. The earliest records of the CME/flare-related blast wave in the literature can be found in the works of Wagner (1982), Wagner & MacQueen (1983), and Gary et al. (1984). However, the low spatial and temporal resolutions of these earlier studies cannot rule out the possibility that the shocks were CME-driven.

Furthermore, observations of type II and III bursts indicate that while type III bursts may appear at any altitude, from the very low corona (corresponding to gigahertz frequencies) to interplanetary space (corresponding to kilohertz frequencies), type II bursts do not behave the same way: the reported highest frequencies of the fundamental components of type II bursts usually do not exceed a few hundred MHz (e.g., see Kundu 1965; Zlotnik et al. 1998; Klassen et al. 2000; Dulk et al. 2000; Cane et al. 2002; Klassen et al. 2003; Mann et al. 2003). This suggests a minimum altitude at which type II emission could be excited. On the basis of the empirical model of the plasma density in the corona given by Sittler & Guhathakurta (1999), a frequency of 200 MHz corresponds to an altitude of 0.37 $R_\odot$, or 2.6×10^5 km from the solar surface, which is close to the maximum height that the postflare loop system could reach near the end of a typical flare process (e.g., Švestka 1996; Lin 2002).

Finally, it has been known for decades that about 50% of type II bursts are preceded by a group of type III bursts by several minutes (e.g., Kundu 1965, p. 339). Recently it has been shown that the overall frequency envelope of the precursor type III bursts drifts at a rate close to that of the associated type II bursts (Klassen et al. 1999; Klassen & Pohjolainen 2002). These type III bursts usually take place in the impulsive phase of the flare and are located between the site of the impulsive energy release and the associated type II bursts (e.g., Klassen et al. 2003). This makes sense if a reconnecting current sheet is located between the solar flare and the associated CME: the type II burst is invoked by the CME-driven shock, and the beam of energetic particles accelerated by the electric field in the current sheet is responsible for the type III burst.

On the basis of the above arguments, it seems, at least to us, that the CME-driven shock plays a much more important role in exciting the type II radio bursts than any flare-related blast wave. A CME has to take off from a stationary configuration. Therefore, a CME-driven shock cannot be produced until the CME velocity exceeds the local magnetoacoustic speed. Usually, fast magnetohydrodynamic (MHD) shocks are expected to form when the CME front speed v_F exceeds the local fast-mode speed V_f in the corona, where

$$V_f^2 = V_{\rm A}^2\left[\frac{1+\beta}{2} + \frac{\sqrt{(1+\beta)^2 - 4\beta\cos^2\alpha}}{2}\right], \qquad (1)$$

$V_{\rm A}$ is the local Alfvén speed, $\beta = (V_s/V_{\rm A})^2$ is a factor of 1.2 smaller than the commonly used plasma β (V_s is the local sound speed), and α is the angle between the magnetic field and the propagation direction of the shock. For the force-free or low-β corona ($\beta \ll 1$), V_f is identified with $V_{\rm A}$, which depends on both the local magnetic field and the plasma density and declines with increasing distance after peaking in the low corona (e.g., Lin 2002). As the CME accelerates and the value of $V_{\rm A}$ drops, it becomes more likely that the CME can drive a shock.

It is, however, difficult to prove that all coronal shocks observed are driven by CMEs (Cane & Erickson 2005; Pohjolainen & Lehtinen 2006; Vršnak et al. 2006). The detailed process through which the shock that produces the type II radio burst may be ignited is still of the subject of active research, so no hard and fast conclusions can yet be drawn. In the present work, we focus on the shocks that are driven by CMEs. We quantitatively investigate the altitudes at which v_F exceeds V_f; namely, the onset positions of type II radio bursts. Both v_F and V_f depend on variations of plasma and magnetic field in the corona, and thus so do the onset positions. The main task of the present work is to seek such a dependence and to study dynamical behaviors of the related parameters on the basis of the catastrophe model of solar eruptions.

In the next section, we briefly summarize the model and some key parameters and results from our previous work. In § 3, we calculate the onset positions, times, and start frequencies of type II radio bursts for various background fields and rates of magnetic reconnection. In § 4, we study properties of the electric field induced by magnetic reconnection in the current sheet, and the possible implications to the associated flare and type III bursts are discussed as well. Finally, we discuss the results and give our conclusions in § 5.

2. SUMMARY OF THE CATASTROPHE MODEL

In the framework of the catastrophe model, the coronal magnetic field is initially in equilibrium and keeps evolving in response to the continuous motion of the photospheric material because the coronal field is rooted in the photosphere. Due to the long timescale (a few days) of the photospheric motion, the coronal magnetic field remains in quasi-static equilibrium for a while until the critical point is reached, beyond which the equilibrium breaks down and the consequent evolution is dynamic. Such a transition in the system's evolution from quasi-static to dynamic constitutes the "catastrophe" (e.g., see Forbes 2000, Priest & Forbes 2002, and Lin et al. 2003 for reviews).

The magnetic configurations in the catastrophe model depicted in Figure 1 assume a geometry in which the prominence, the flux rope, and the CME core are colocated. This is done for mathematical convenience, although in some observed CMEs these structures do seem to be colocated. The equilibrium in the magnetic configuration is realized when the magnetic compression and tension forces acting on the flux rope balance each other. The magnetic compression results from magnetic field lines between the flux rope and the photosphere (or the boundary surface), and the magnetic tension is in the field lines that pass over the top of the flux rope and are anchored in the photosphere. The upward motion of the flux rope is therefore driven by the magnetic compression force, and the flux rope is thrust outward as tension loses to compression.

Lin & Forbes (2000) constructed an analytic model of solar eruptions that investigated how magnetic reconnection affects the CME acceleration and how the acceleration in turn affects the reconnection process. The role of magnetic reconnection in the eruption is threefold: first, it helps the flux rope to escape smoothly into interplanetary space, developing into the CME; second, it creates the growing flare loops in the corona, the separating flare ribbons on the disk (e.g., see Forbes 2003), and the CME bubbles, which expand rapidly as the CME propagates in space (Lin et al. 2004); and third, its non-ideal MHD properties imply that the problem of opening the closed magnetic field by a purely ideal MHD process in the force-free environment, also known as the Aly-Sturrock paradox (Aly 1991 and Sturrock 1991), which was first raised by Aly (1984), is naturally avoided (e.g., Forbes 2000; Klimchuk 2001; Lin et al. 2003).

Incorporating the plasma mass in the flux rope to the catastrophe model, Lin (2004) studied the impact of gravity on both the triggering and the traveling of a CME. The results showed that for a prominence containing 2.1×10^{16} g of plasma initially, which is close to the upper limit of the total mass that a major CME can bring into interplanetary space (Howard et al. 1985, 1997; D. F. Webb 2003, private communication), the effect of gravity is negligible unless the background field on the boundary surface in the disrupting configuration is weak enough, say, weaker than 30 G. Otherwise, evolutions in the system in both the quasi-static and the dynamic phases are uniquely governed by the magnetic field. Furthermore, Lin (2004) realized that the background field also determines the correlation of the solar flare to the associated CME: the stronger the background field, the better the flare correlates to the CME; otherwise, the correlation is poor. Because the background field governs many important parameters describing an eruptive process, such as the CME speed, the onset of magnetic reconnection, the electric field in the current sheet, and the output power of the eruptive process (e.g., see Lin 2002, 2004), it should affect the onset positions and times of radio bursts of types II and III as well. In §§ 3 and 5 below, we quantitatively look into how the onset times and positions of radio emissions vary with the background field and other related parameters on the basis of the catastrophe model of solar eruptions. Consequently, the correlations of two types of radio bursts will also be investigated. In addition to those mathematical notations shown in Figure 1, we follow our

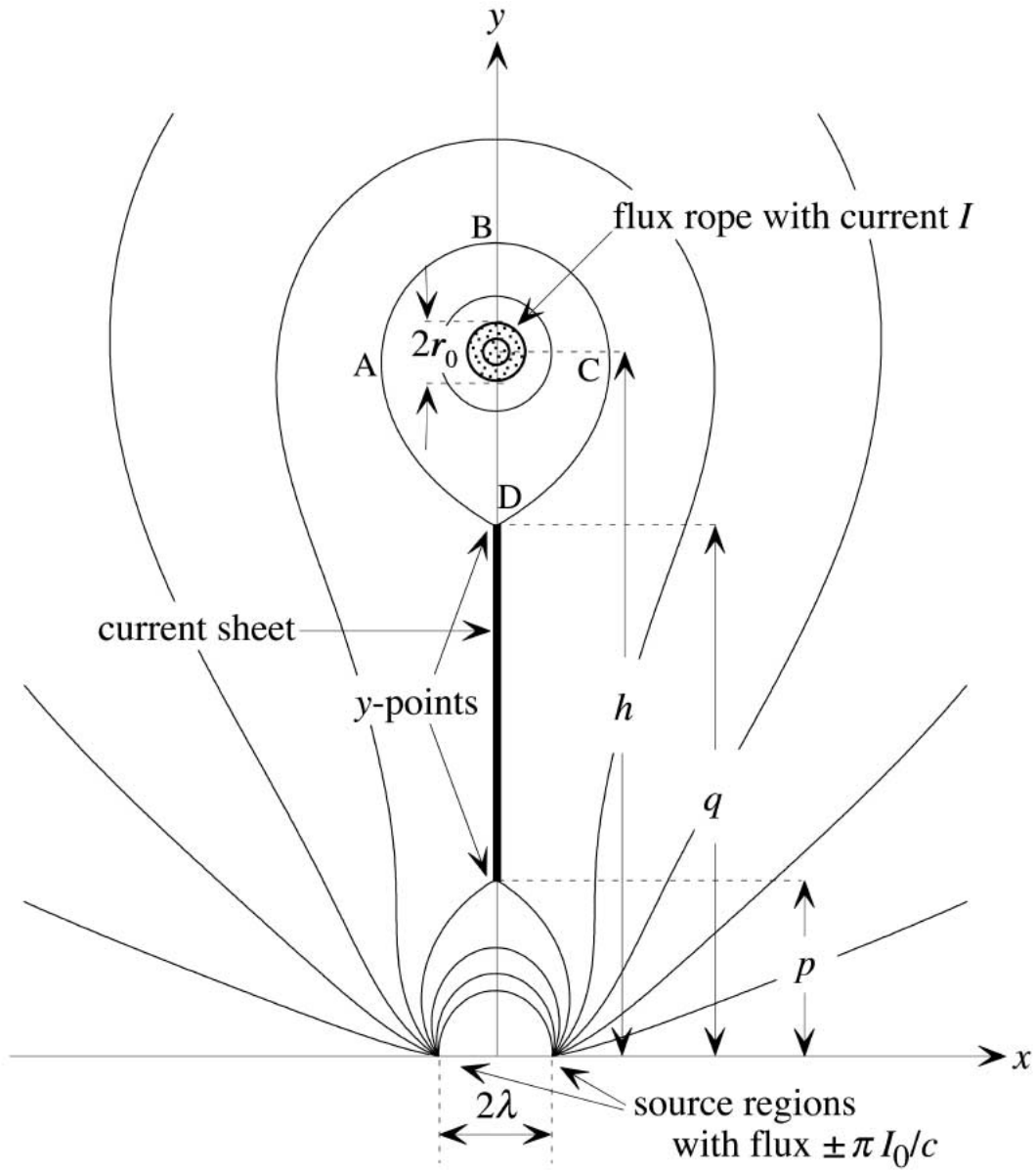

FIG. 1.—Diagram of the flux rope configuration, showing the mathematical notation used in the text (from Lin & Forbes 2000). The x-axis is located on the solar surface, and the y-axis points upward. The height of the center of the flux rope is denoted by h, p and q denote the lower and upper tips of the current sheet, respectively, and the distance between the magnetic source regions on the photosphere is 2λ.

previous practice of using B_0 for the magnetic field at the origin and using E_z for the electric field induced in the current sheet (see Lin 2002, 2004).

2.1. *Important Formulae*

Before studying the properties of type II and type III radio bursts, we investigate CME propagations in various situations. We start by arranging the equations that govern the dynamical behaviors of the disrupting magnetic field. In the work of Lin (2004), the impact of gravity on the CME propagation was studied and that of increasing mass in the CME bubble was ignored; in the works of Lin et al. (2004) and Lin & Soon (2004), on the other hand, the alternative occurred. In the present work, the impact of both gravity and increasing mass will be incorporated in our calculations. Some important parameters investigated in this work are specified in Figure 1. Generally, the magnetic field shown in Figure 1 is not necessarily in equilibrium, especially since the configuration includes a reconnecting current sheet. The following characteristic values of the above parameters are set for the purpose of normalization:

$$\lambda_0 = 5\times10^4 \text{ km}, \quad m_0 = 2.1\times10^6 \text{ g cm}^{-1},$$
$$r_{00} = 0.1\lambda_0, \quad \rho_0 = 1.673\times10^{-14} \text{ g cm}^{-3},$$
$$I_0/c\lambda_0 = 50\sigma \text{ G}, \quad \dot{h}_0 = 10^3 \text{ km s}^{-1},$$

where the value of $2\lambda_0$ adopted is appropriate for a prominence before the eruption (Priest 1982), I_0 is a constant in units of electrical intensity, m_0 is the initial mass per unit length inside the flux rope, which is also used to normalize the total mass per unit length m, r_{00} is the initial value of the flux rope radius (Fig. 1), $B_0 = 2I_0\sigma/c\lambda_0$ is the background field strength at the origin, σ is the corresponding relative strength, ρ_0 is the plasma density at the base of the corona, and $\dot{h}_0$ is used to normalize the flux rope velocity $\dot{h}$.

By combining the results of Lin et al. (2004) and Lin & Soon (2004) with those of Lin (2004), we obtain a set of ordinary differential equations that govern the dynamical evolution of a rapidly expanding CME bubble that includes a flux rope:

$$\frac{dp}{dt} = \frac{6}{5}p'\dot{h}, \quad \frac{dq}{dt} = \frac{6}{5}q'\dot{h}, \tag{2}$$

$$\frac{d\dot{h}}{dt} = \frac{6}{5}\dot{h}'\dot{h}, \quad \frac{dh}{dt} = \frac{6}{5}\dot{h}, \tag{3}$$

$$\dot{h}\dot{h}' = \frac{3.125\lambda^2\sigma^2}{2.1mhL_{PQ}^2} \times \left[\frac{H_{PQ}^2}{2h^2} - \frac{(\lambda^2+p^2)(h^2-q^2)}{\lambda^2+h^2} - \frac{(\lambda^2+q^2)(h^2-p^2)}{\lambda^2+h^2}\right] - \frac{1.37\times10^{-2}}{(1+5h/69.6)^2} \tag{4}$$

and

$$\frac{dm}{dt} = 1.04204\, M_A\sigma \frac{\lambda(q-p)(h^2+\lambda^2)}{(h^2-y_0^2)(y_0^2+\lambda^2)}\sqrt{\frac{f(y_0)(q^2-y_0^2)(y_0^2-p^2)}{(p^2+\lambda^2)(q^2+\lambda^2)}}, \tag{5}$$

where $L_{PQ}^2 = (\lambda^2+p^2)(\lambda^2+q^2)$, $H_{PQ}^2 = (h^2-p^2)(h^2-q^2)$, the prime ($'$) indicates the derivative with respect to h, $y_0 = (p+q)/2$, t is the time in units of minutes, and M_A is the rate of magnetic reconnection measured in terms of the reconnection inflow speed compared to the local Alfvén speed near the current sheet. All the lengths have been normalized to λ_0, masses to m_0, and speeds to $\dot{h}_0$.

Equations (2) describe the evolution of the current sheet, equations (3) and (4) describe the motion of the CME bubble, and equation (5) determines the change of the total mass inside the CME bubble. The expressions for p', q', and $\dot{h}'$ given by Lin & Forbes (2000) are summarized in the Appendix.

In our calculations, the coronal plasma density $\rho(y) = \rho_0 f(y)$ is taken from the empirical model of Sittler & Guhathakurta (1999), such that

$$f(y) = a_1 z^2(y) e^{a_2 z(y)}\left[1 + a_3 z(y) + a_4 z^2(y) + a_5 z^3(y)\right], \tag{6}$$

$$z(y) = 1/(1+y), \quad a_1 = 0.001272,$$
$$a_2 = 4.8039, \quad a_3 = 0.29696,$$
$$a_4 = -7.1743, \quad a_5 = 12.321,$$

with $f(0) = 1$. The function $f(y)$ in equation (6) describes an isothermal atmosphere at lower altitudes ($<0.7\ R_\odot$), which then decreases quadratically with height in the outer corona and in interplanetary space.

We are now ready to investigate various observational consequences manifested by a disrupting system that is governed by equations (2)–(5). During the eruption, the time $t = 0$ is set at the moment when the flux rope starts to lose its mechanical equilibrium; namely, when the catastrophe begins. For the magnetic configuration we are working on, magnetic reconnection does not occur until $t = t^*$, when a neutral point appears at the boundary surface and a current sheet begins to develop (refer to Lin & Forbes 2000 and Lin 2002 for more details). So the initial time for integrating equations (2)–(5) is at $t = t^*$, and these equations are solved with initial conditions

$$t = t^*, \quad h = h^*, \quad \dot{h} = \dot{h}^*,$$
$$m = m^* = 1, \quad p = p^* = 0, \quad q = q^* = 0. \tag{7}$$

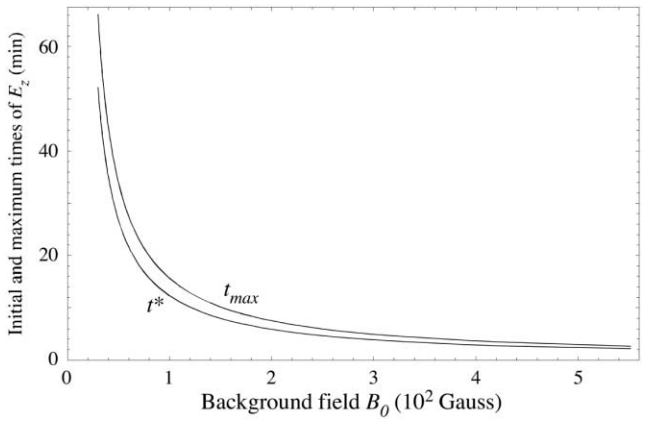

FIG. 2.—Variations of the E_z initial time, t^*, and the time when E_z is at maximum, t_{max}, vs. the background field B_0 (or σ).

According to Lin (2002), t^* and $\dot{h}^*$ are roughly proportional to $1/\sigma$ and σ, respectively, if the gravity of the plasma inside the flux rope is neglected. When gravity is considered, however, the above dependences become complex, especially in the case of a weak background field (say, $\sigma < 30$ G; Lin 2004). The time $t = t^*$ specifies the moment when the current sheet starts to form and magnetic reconnection is initiated inside the current sheet (e.g., Lin & Forbes 2000). Thus, it also indicates when the associated flares in the eruption commence. In the present work, the values of t^* and $\dot{h}^*$ will be determined via the approaches developed by Lin (2004) for various values of σ.

Figure 2 plots variations of t^* against σ for $M_A = 0.1$. Because the existence of the electric field E_z in the current sheet is an alternative indication that magnetic reconnection occurs and t^* is also the initial time of E_z, we also plot the time t_{max}, at which the electric field E_z is at maximum, against σ in Figure 2 for comparison. Their observational consequences related to flares and type II and type III radio bursts, as well as the correlations among them, will be discussed later.

When investigating the effects of magnetic reconnection on the onset of radio bursts in our subsequent calculations, we assume that M_A is constant and set it equal to either 0.05 or 0.1. Generally speaking, M_A is a function of both time and the properties of the plasma and magnetic field around the reconnection site, such as the length and thickness of the current sheet, the strength of the magnetic field, and the plasma resistivity. Since there is no commonly accepted, rigorous theory for how fast reconnection occurs when driven by a catastrophic loss of equilibrium in the magnetic field, we assume that M_A is a constant of less than unity in our calculations. For detailed discussions of the functional behaviors and plausible values of M_A, see Lin & Forbes (2000) and Forbes & Lin (2000). Recent observations also suggest that the values of M_A that we use for the present work are not bad choices (e.g., Yokoyama et al. 2001; Ko et al. 2003; Lin et al. 2005).

Our calculations show that the extra mass added to the CME bubble during the eruption, which is governed by equation (5),

enhances the impact of gravity on the CME propagation. The CME motion suffers from deceleration for $\sigma \leq 0.685$ when $M_A = 0.05$, and deceleration occurs for $\sigma \leq 0.423$ when $M_A = 0.1$. This indicates that the excess material injected into the CME bubble increases the thresholds of both the background field and the rate of magnetic reconnection for smooth propagation of CMEs.

2.2. *Various Components of CME Speeds*

We need to find the component of the CME speed that is responsible for igniting shocks. We denote this speed component as v_F. Thus, the onset positions of type II radio bursts are determined by comparing v_F to the local Alfvén speed, V_A, in the force-free environment (refer to eq. [1]), and the CME-driven shock forms when v_F exceeds V_A. Because the CME is accelerated from rest following the takeoff of the eruption, it takes v_F a while to surpass V_A, if it eventually can. Therefore, we do not expect type II radio bursts to appear at lower altitudes.

Lin & Soon (2004) and Lin et al. (2004) calculated the time profiles of various parameters for the CME bubble and the flux rope. The profiles suggest that expansion of the CME bubble is fairly rapid, much faster than the adiabatic expansion of the flux rope itself, and that the "flux rope" that is often observed during the eruption is very likely the expanding bubble, instead of the flux rope that is usually used to model the filament or prominence in the catastrophe model.

Expansion of the CME bubble mainly results from magnetic reconnection: it is not caused by mass motions of the related plasma, but rather by the continual propagation of the magnetic separatrix onto new field lines, which is exactly like what happened to the flare loop system (e.g., Schmieder et al. 1987; Forbes & Acton 1996). Thus, according to our model, it is the velocity of the flux rope that needs to be taken into account for the shock creation, and the shock is most likely to form in front of point B in the configuration shown in Figure 1. The CME velocity $\dot{h}$ that is deduced by integrating equations (2)–(5) with the initial conditions given in equations (7) could be an upper limit, since we treat the CME as a projectile in our calculations (e.g., Lin & Forbes 2000), and all the magnetic energy released is assumed to be used in speeding up the CME. Recently, Reeves & Forbes (2005) studied the heating features associated with CME motions and found that including the thermal energy and evaporation in the catastrophe model does not change our previous results because only the work done by the magnetic force on the flux rope affects the trajectories.

Having carefully reinvestigated their ways to approach the related problems, we noted that the issues regarding heating and kinetic energy in the eruption were still dissociated from one another in the work of Reeves & Forbes (2005). So, in the present work, we follow our previous practice (Lin 2002, 2004) of assuming that half of the released magnetic energy goes to heating and the other half goes to the kinetic energy of the CME. As for the accurate partition of the released energy, the debate is still on: in some events the kinetic energy is dominant (Emslie et al. 2004), in some events the heating is dominant (Sui et al. 2005), and in some others they are equal (Akmal et al. 2001; Ciaravella et al. 2001). Thus, for simplicity, we treat them equally in our calculations.

Allowing half of the released energy to heat the atmosphere decreases the CME velocity by a factor of $\sqrt{2}$; therefore, the more accurate expression of v_F becomes

$$v_F = \dot{h}/\sqrt{2}, \tag{8}$$

where $\dot{h}$ is calculated from equations (2)–(5) with the initial conditions given in equations (7). To determine the onset positions and times of the type II radio bursts, we also need to calculate the local Alfvén speed at the front edge of the CMEs, namely, at point B in Figure 1.

The magnetic configuration shown in Figure 1 is described by (e.g., Lin 2001)

$$B_y + iB_x = \frac{2iI_0\sigma\lambda\left(h^2+\lambda^2\right)\sqrt{(z^2+p^2)(z^2+q^2)}}{c\left(z^2-\lambda^2\right)(h^2+z^2)\sqrt{\left(\lambda^2+p^2\right)\left(\lambda^2+q^2\right)}}, \tag{9}$$

where B_x and B_y are the x- and y-components of the magnetic field, $i = \sqrt{-1}$, and $z = x + iy$. The magnetic field near point B is mainly in the x-direction, and

$$B_x|_{x=0,\,y=y_B} = \frac{2I_0}{c\lambda_0}\frac{\sigma\lambda\left(h^2+\lambda^2\right)\sqrt{(y_B^2-p^2)(y_B^2-q^2)}}{\left(y_B^2+\lambda^2\right)(y_B^2-h^2)\sqrt{\left(\lambda^2+p^2\right)\left(\lambda^2+q^2\right)}}.$$

Then we find the local Alfvén speed at point B,

$$V_A(y_B) = \frac{2I_0}{c\lambda_0\sqrt{4\pi\rho_0}}\frac{\sigma\lambda\left(h^2+\lambda^2\right)}{\left(y_B^2+\lambda^2\right)(y_B^2-h^2)}\sqrt{\frac{\left(y_B^2-p^2\right)\left(y_B^2-q^2\right)}{f(y_B)\left(\lambda^2+p^2\right)\left(\lambda^2+q^2\right)}}. \tag{10}$$

Here we note that the most likely location at which the CME-driven shock is first ignited is in front of the CME bubble in our simple model (refer to Fig. 1); in reality, on the other hand, the CME might move and expand asymmetrically (see Klimchuk 2001 for some examples). So the onset positions of the shock and thus the type II bursts may vary from CME to CME: sometimes in the front and other times at the flanks. Discussions with more details on this issue can also be found in the works of Gopalswamy et al. (2001b) and Mann et al. (2003).

3. ONSET POSITIONS AND TIMES OF TYPE II BURSTS

When v_F and V_A are known, we are able to locate the onset positions of type II radio bursts by comparing v_F and V_A, both of which are functions of time and altitude. Figure 3 displays four panels plotting v_F and V_A against height (lower x-axis ticks) and time (upper x-axis ticks) for various values of σ and M_A. Arranging the x-axis labels and legends this way helps us locate and time the onset of radio bursts easily. Because neither h nor y_B is a linear function of time, especially at the early stage of the eruption, the distribution of the upper x-axis ticks (for time) is not uniform, but we set the lower ones (for altitude) uniformly.

In Figures 3*a* and 3*d*, the corresponding plasma frequency f_{pe} at the front point of the CME (see point B in Fig. 1), which is given by

$$f_{pe}(y) = 0.898408\sqrt{f(y)}|_{y=y_B}\ (\mathrm{GHz}), \tag{11}$$

is also included. Frame ticks for the y-axis in these two panels are arranged such that the left labels and legends are for velocities and the right ones are for the corresponding values

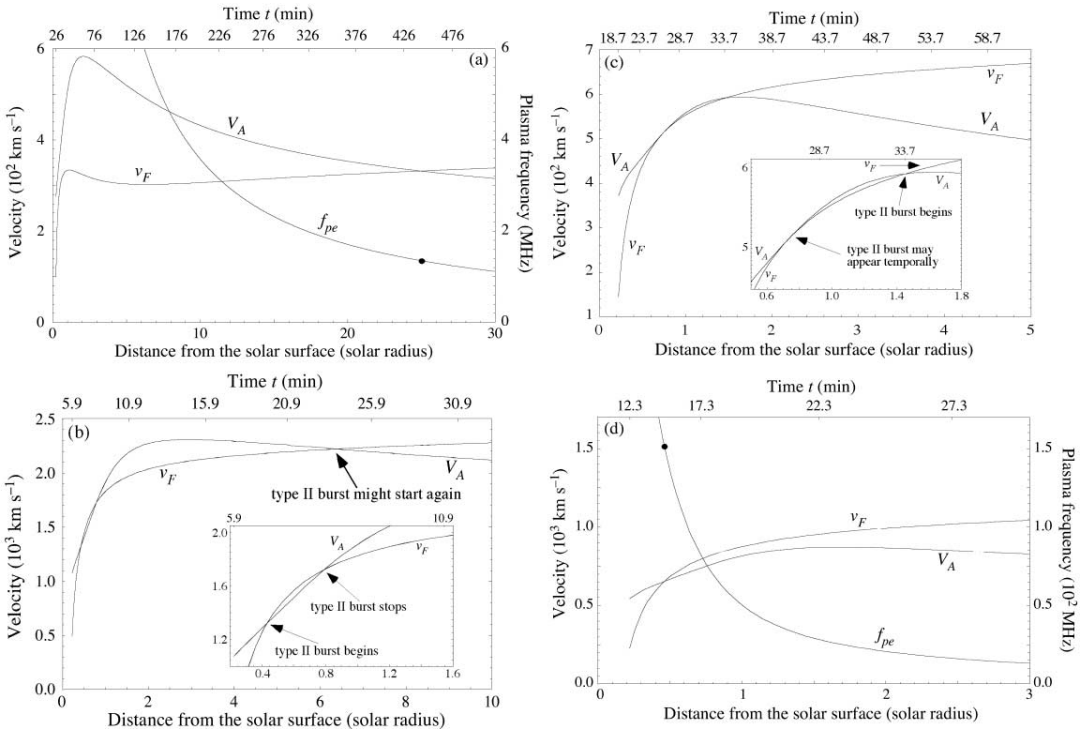

FIG. 3.—Variations of the CME front velocities, v_F, and the local Alfvén speed, V_A, vs. height and time for different background fields and rates of magnetic reconnection: (*a*) $M_A = 0.05$ and $\sigma = 0.5$, (*b*) $M_A = 0.05$ and $\sigma = 2$, (*c*) $M_A = 0.1$ and $\sigma = 0.69$, and (*d*) $M_A = 0.1$ and $\sigma = 1$. The corresponding plasma frequencies f_{pe} at the CME front are also plotted in (*a*) and (*d*) to demonstrate how f_{pe} varies with altitude. The insets in (*b*) and (*c*) show more details of the critical regions and use the same units.

of f_{pe}. Two filled circles on the f_{pe} curves, one in each panel, indicate the position and the time at which v_F exceeds V_A. Thus, the segments of the f_{pe} curves to the right of the filled circles should depict the main feature of the fundamental lane of type II bursts that is usually seen in the dynamic spectra of radio emissions.

In Figures 3*b* and 3*c*, we note that the behavior of v_F compared to V_A becomes more complex than those shown in the other panels. The two curves meet at two or even three places, which implies richer manifestations of the type II bursts in the eruption. The inset in each panel is used to show more details of the v_F and V_A curves in the critical region. Detailed discussions on the relevant issues will be given soon.

All plots in Figure 3 indicate that v_F is less than V_A at lower altitudes and in the early phase of the eruption, and that the situation reverses as h and y_B get larger. We note that the positions at which v_F surpasses V_A depend in an apparent way on both σ and M_A. For slow magnetic reconnection ($M_A = 0.05$) and a weak field (say, $\sigma < 0.5$), v_F exceeds V_A when the CME is far from the Sun (Fig. 3*a*). In this case, we see a single intersection between v_F and V_A curves at large altitude and expect the type II burst to appear at low frequencies as the CME becomes distant.

In principle, both v_F and V_A depend on σ and increase with σ. Thus, Figure 3 shows that the v_F and V_A curves move upward in the plots as σ gets bigger. But v_F increases slightly faster than V_A; therefore, v_F starts to exceed V_A, and the type II radio bursts may be expected at lower altitudes for $\sigma = 2$ (Fig. 3*b*). On the other hand, different behaviors of v_F and V_A against h and t yield that the variation of v_F compared to V_A in the eruptive process is not monotonic, and the case may happen in which v_F is surpassed by V_A again somewhere at higher altitudes and the radio bursts cease at these heights. Due to the fact that V_A decreases monotonically at high altitudes, we may expect the type II bursts to resume later as the CME propagates farther away.

In addition to depending on σ, v_F is also a function of M_A. We have known that large values of M_A mean a fast CME (e.g., Lin & Forbes 2000; Forbes & Lin 2000; Lin 2002). Thus, increasing M_A allows v_F to be able to reach V_A in the lower corona even if σ is not very large (see Fig. 3*c*). Eventually, v_F overwhelms V_A at large distances. Therefore, in the cases shown in Figures 3*b* and 3*c*, we should be capable of observing the type II burst switching on at lower altitudes earlier, switching off after a while, and then switching on again as the CME becomes farther away later on.

Coinciding with our intuition, the eruption taking place in the strong field ($\sigma \geq 1$) with fast magnetic reconnection ($M_A = 0.1$) speeds up the CME in a significant way such that v_F gets larger than V_A at lower altitudes in the early phase of the eruption, and type II radio bursts occur with the higher start frequency (Fig. 3*d*). The time profiles of various parameters for the CME bubble given in Figure 5 of Lin & Soon (2004) indicate that the apparent acceleration of CME commences with the formation of the current sheet and the initiation of reconnection. Thus, v_F does not exceed V_A and type II radio bursts do not start earlier than the formation of the current sheet. Because the type II burst is produced by the CME-driven shock, the location of the CME front, y_B, determines the onset positions of the burst. The current sheet starts to form and reconnection begins at $t = t^* \approx 12$ minutes and $y_B \approx 0.2\ R_\odot$ for $\sigma = 1.0$ and $M_A = 0.1$. The values of t^* and the corresponding values of y_B depend on σ such that both of them vanish as σ goes to infinity (see also Fig. 2), but they are approximately tens of minutes and a few tenths of the solar radius, respectively, for $M_A = 0.1$ and $\sigma = 1.0$, which may correspond to the typical

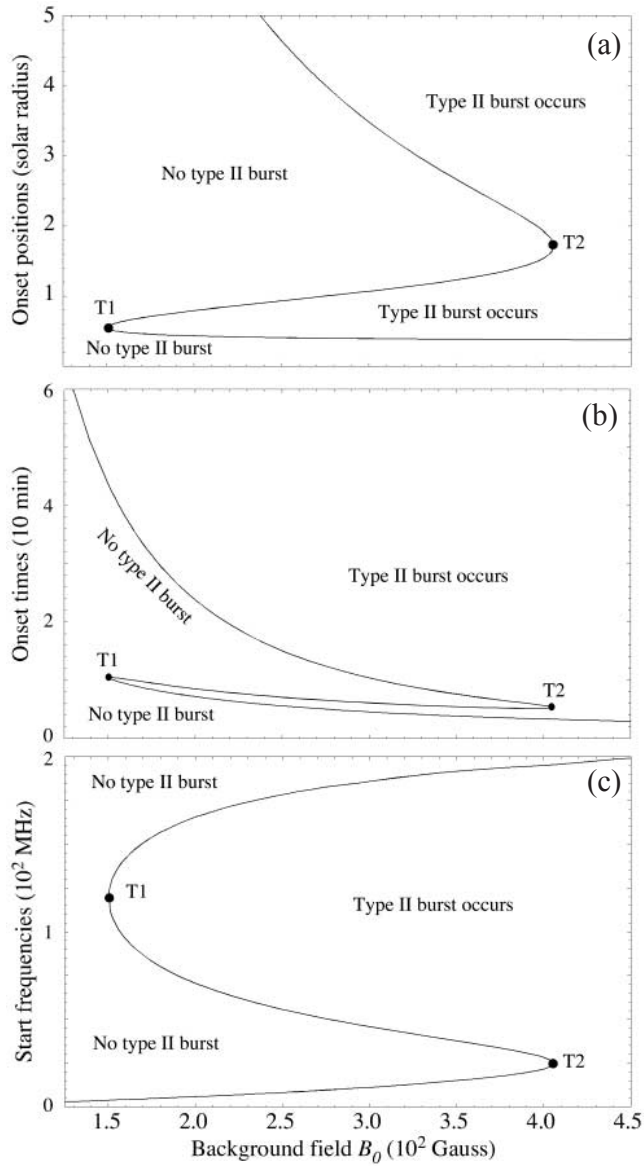

FIG. 4.—Positions (*a*), times (*b*), and frequencies (*c*) at which v_F exceeds V_A as functions of σ for $M_A = 0.05$. Two turning points at each of these curves are explicitly marked.

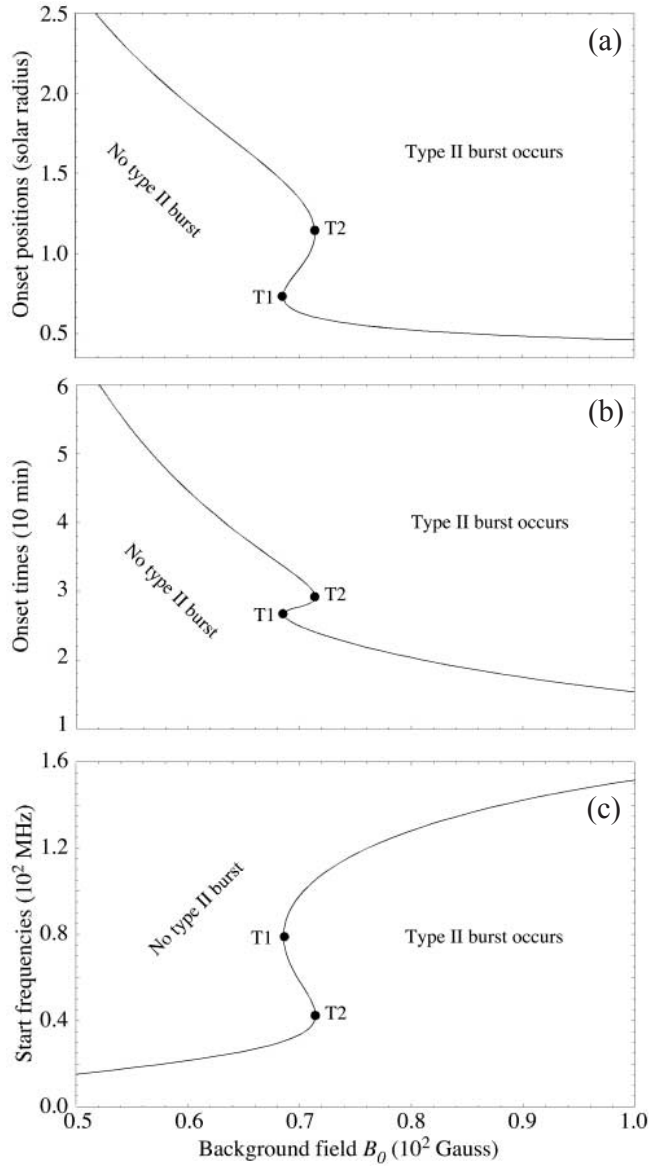

FIG. 5.—Same as Fig. 4, but for $M_A = 0.1$.

major eruptions. Therefore, the start frequencies of the fundamental lanes of the type II burst are generally lower than 200 MHz.

Before continuing, we need to note that there is not a universally accepted standard for M_A to distinguish fast and slow magnetic reconnections in the realistic eruptive event. Theoretically, Lin & Forbes (2000) and Lin (2002) found that magnetic reconnection with $M_A = 0.1$ always leads to fast energy conversion that may result in a major flare and a fast CME in the realistic coronal environment, and that when M_A becomes small (say, less than 0.01), the energy conversion becomes difficult and the relevant eruption may even be prevented and the associated CME stops propagating. A couple of failed eruptive events have actually been reported (Filippov & Koutchmy 2002; Ji et al. 2003).

Yokoyama et al. (2001) found that the value of M_A for a gradual event ranged from 0.001 to 0.01, and Ko et al. (2003) and Lin et al. (2005) found that its value for major events ranged from 0.01 to 0.1. In the present work, we investigate the response of the disrupting magnetic field of interest when decreasing M_A, but we also avoid the case in which M_A is too small to allow the eruption to develop smoothly. So we define, with some arbitrariness, that magnetic reconnection with $M_A = 0.1$ is fast and that with $M_A = 0.05$ is slow.

Having obtained the curves in Figure 3, we realize that intersections of the v_F and V_A curves vary with both σ and M_A. Collecting those values at intersections for different values of σ and M_A allows us to investigate the height y_B and the frequency f_{pe}, as well as the time t_{in} at which the type II burst takes place, as functions of M_A and σ. Figures 4*a*, 4*b*, and 4*c* plot the values of such y_B, f_{pe}, and t_{in} against σ for $M_A = 0.05$, respectively, and Figure 5 displays the same functions for $M_A = 0.1$. In each panel of the two figures, we denote the area where type II bursts occur with "Type II burst occurs" and that where type II bursts are prohibited with "No type II burst." Corresponding to the cases shown in Figures 3*b* and 3*c*, variations of y_B, t_{in}, and f_{pe} versus σ are not monotonic if the values of σ are within the range between the turning points T1 and T2 denoted on each curve in Figures 4 and 5. The curves shown in Figure 3*c* are for the critical case in

which σ takes the value at point T1 in Figure 5. For the eruption that takes place in the magnetic structure with σ in this region, one may expect that the type II burst occurs at an early stage of the eruption with higher start frequencies, disappears later on as the CME gets higher, and then may resume when the CME reaches much larger altitudes. Such a behavior of type II radio bursts was indeed observed (Gopalswamy et al. 2001a).

A general conclusion that we can draw from Figures 4 and 5 is as follows: v_F may exceed V_A easily if the eruption happens in an environment with large σ (refer to the domain of σ at the right of point T2 on each curve in Figs. 4 and 5). In this case, type II bursts are expected to begin at lower altitudes (around 0.2–0.7 $R_\odot$ from the solar surface; Figs. 4*a* and 5*a*). Correspondingly, the onset of the bursts following the triggering of the eruption is relatively early, varying from a few minutes to around 20 minutes (Figs. 4*b* and 5*b*), and the start frequencies of the bursts are high, ranging from 80 to 200 MHz (Figs. 4*c* and 5*c*). As for the eruption from the magnetic structure in an environment with small σ (in the σ domain at the left of point T1 in each panel of Figs. 4 and 5), v_F may not be able to exceed V_A until the CME propagates to large distances (around 9 $R_\odot$ for $M_A = 0.05$ and 1.5 $R_\odot$ for $M_A = 0.1$), which are related to the low start frequencies (<4 MHz for $M_A = 0.05$ and <30 MHz for $M_A = 0.1$) and the late onsets ($t_{in} > 43$ minutes for $M_A = 0.05$ and $t_{in} > 30$ minutes for $M_A = 0.1$).

However, we note that the possibility exists for small values of σ that a type II burst does not appear at all. Comparing Figures 4 and 5, we find that this case is more likely to happen if reconnection is slow. Figure 4*a* indicates that v_F would eventually surpass V_A at large distances and very late times, but this does not necessarily mean that type II bursts could actually take place, because it is V_f, given in equation (1), that v_F needs to exceed in order to invoke type II bursts. In the lower corona, $V_f \approx V_A$ as a result of the force-free environment ($\beta \ll 1$). As the altitude gets higher (say, beyond 2.5 $R_\odot$), however, the gas pressure becomes greater than the magnetic compression, and the force-free environment no longer exists ($\beta \geq 1$). In this case, even if v_F can exceed V_A, it may not be able to surpass V_f and invoke type II bursts. Furthermore, observations indicate that fast CMEs usually underwent a deceleration process during propagation, which enhances the difficulty for v_F to exceed V_f. These facts imply that fast CMEs ($v_F \geq 800$ km s^{-1}) in some circumstances may not necessarily be able to produce type II radio bursts. Such CMEs are usually known as radio-quiet fast CMEs and have been observed in many events (Gopalswamy 2004b, pp. 223–224, and references therein).

4. RECONNECTING ELECTRIC FIELD AND FEATURES OF TYPE III BURSTS

Another important parameter in the eruption that we need to discuss is the electric field E_z induced by magnetic reconnection in the current sheet. Like M_A, E_z also measures the rate of magnetic reconnection inside the current sheet. Since it has dimensions of the electric field, it is also known as the absolute rate of magnetic reconnection, compared to M_A, which is known as the relative one (Lin & Forbes 2000). In our calculations, we usually assume that the relative rate M_A is constant, but E_z is not. According to Lin & Forbes (2000) and Lin (2002), E_z is given by

$$E_z = \frac{M_A B_y^2(0, y_0)}{c\sqrt{4\pi\rho_0 f(y_0)}}, \tag{12}$$

where B_y can be obtained from equation (9), and E_z is evaluated at the midpoint y_0 of the current sheet for simplicity. Justifications of such an approach can be found in the works of Lin et al. (2004) and Lin & Soon (2004).

The overall evolutionary behaviors of E_z weakly depend on $f(y)$, and its strength roughly varies with σ quadratically, as implied by equation (12) (Lin & Forbes 2000; Lin 2002). Here we study the other properties of E_z and the corresponding observational consequences.

The role of E_z in the eruption is twofold. First of all, E_z is the absolute rate of the energy conversion through magnetic reconnection and directly governs the evolution of various manifestations of solar eruptions, including brightenings of the flare region (Forbes & Malherbe 1991; Yokoyama & Shibata 1994; Miyagoshi & Yokoyama 2004), motions of the flare ribbons and loops (Lin et al. 1995; Forbes & Acton 1996), the time at which the flare reaches its maximum (Qiu et al. 2004), and dynamic features of the associated CMEs (Lin 2002; Jing et al. 2005).

Secondly, charged particles, especially electrons and protons, can be easily accelerated by E_z in the current sheet (Litvinenko 1996, 2003; Wood & Neukirch 2005 and references therein), and the beam of energetic particles is responsible for type III radio bursts (Kundu 1965; Cane et al. 2002; Gopalswamy 2004a, p. 307; Pick et al. 2005a, 2005b). As these energetic particles propagate downward, they may also account for the heating of the lower atmosphere and brightening of the flare regions (e.g., Švestka 1976).

Therefore, behaviors of E_z in the eruption should be responsible for several important observational consequences regarding type III radio bursts and solar flares, no matter whether the heating is due to the conduction front or due to the bombardment of energetic particles. We used to utilize the peak time of the CME kinetic power to approximately represent the time of the associated flare at maximum (Lin 2002, 2004), but the above two items suggest that it is more appropriate to use E_z to describe the flare features.

In addition to the time profile of E_z, our work on this issue is also related to the evolution of the current sheet. On the one hand, the current sheet is the product of the eruption as a result of the catastrophe (e.g., Forbes & Isenberg 1991); on the other hand, the current sheet is also an essential region for energy conversion, including particle accelerations. So the trajectories or the motion patterns of energetic particles should be somehow confined and regulated by the size of the current sheet before they escape from the current sheet. In the following subsections, we investigate the implications of the properties of E_z and the current sheet for the behaviors of type III bursts, including those used as precursors of the associated type II bursts (e.g., Klassen et al. 2003), and for the possible correlations of type II bursts to solar flares as well.

4.1. *Impact of the Current Sheet Evolution on Type III Burst Features*

Type III radio bursts are recognized as energetic electron beams that propagate through the coronal or interplanetary plasma. The plasma environment is unstable to such beams, and the corresponding instability excites Langmuir waves in the plasma, which produce radio emissions at the local plasma frequency. The magnetic field plays a role in guiding the electron beams. If the magnetic field is open, electron beams could propagate to very high altitudes, most of the time all the way to the Earth, and the resultant type III burst can be observed on the dynamic spectrum to drift over a wide frequency range from gigahertz to kilohertz (Cane et al. 2002; Gopalswamy 2004a, pp. 307–311). If the field is closed, on the other hand, the motions of electrons

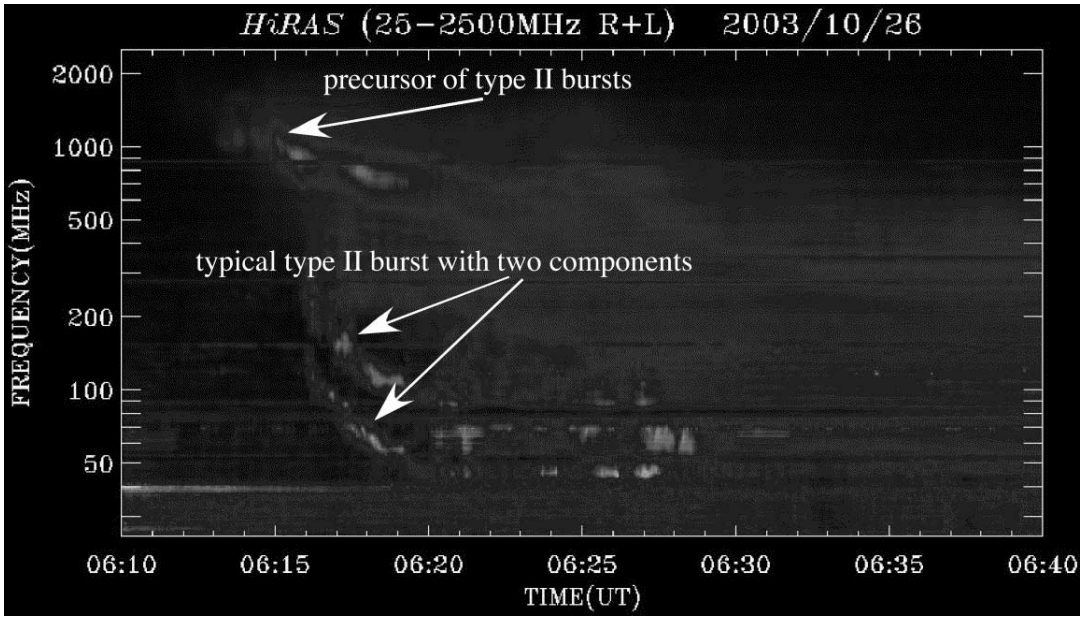

FIG. 6.—Dynamic spectrum of the event observed on 2003 October 26 by HiRAS. Both the type II burst and the precursor on this spectrum can easily be recognized. [*See the electronic edition of the Journal for a color version of this figure.*]

are limited to a local region, and the frequency drift of type III bursts is confined in a small range, which results in the short frequency drift of type III bursts on the dynamic spectrum. Compared to the fully open field, the region of the magnetic field near the current sheet (Fig. 1) is apparently confined. The confinement of such a configuration on the motions of energetic particles can be seen from the behaviors of those type III radio bursts that usually were used as the precursors of the associated type II bursts (e.g., Klassen et al. 2003 and references therein).

In addition to the figures shown in previous works, Figure 6 manifests another example of the precursor and the type II radio burst. It was obtained from the 2003 October 26 event by the Hiraiso Radio Spectrometer (HiRAS; Kondo et al. 1995). This dynamic spectrum in the eruption consists of a decimetric type IV–like envelope of the type III radio bursts and two lanes of the associated type II radio bursts, which represent the emissions at the fundamental frequency ($f = f_{pe}$) and at the harmonic frequency ($f = 2f_{pe}$), respectively. According to Klassen et al. (2003), such an envelope of type III radio bursts constitutes a precursor of the associated type II radio bursts. Like those displayed in previous works, the fine structures in the frequency drift patterns of individual type III bursts are also clearly manifested in Figure 6. Detailed analyses and investigations of this event will be performed in future work.

So far, some common features of the precursors can be summarized from Figure 6 and previous works as follows. First, they are composed of a group of fine structures such that individual components of type III bursts in the envelope are distinguishable from one another; second, the extension of each individual component of type III bursts in the frequency domain is confined in a small range; third, the precursor envelope commences at the lower layers of the atmosphere (or the higher frequencies) and slowly drifts toward the higher layers (or the lower frequencies) during the eruption; and fourth, compared to the precursor, the type II burst itself does not show similar fine structures, and the corresponding frequency drift in the high-frequency range is apparently faster than that of the precursor. Therefore, the drift in the precursor envelope represents a motion pattern different from those represented by either type II or type III bursts.

If we relate the motions of the energetic particles responsible for the precursors to the evolution in the current sheet, especially in its length, $q - p$ (Fig. 1), we realize that the shape of the precursor may represent the current sheet evolution, since the motions of these particles are confined in the current sheet. As indicated by Figure 1, the lower tip of the current sheet, p, is located at the top of the postflare loop system, and the upper tip, q, is at the bottom of the CME bubble. Basically, the evolution of p is governed by magnetic reconnection and that of q is dominated by both the motion of the CME (or flux rope) and magnetic reconnection (Lin & Forbes 2000; Forbes & Lin 2000; Lin 2002).

Soon after the formation of the current sheet, the electrons brought into the current sheet by the reconnection inflow are quickly accelerated by the electric field E_z. At the initial stage, both the CME and the current sheet are located and confined in the lower part of the closed magnetic structure; therefore, the accelerated electrons are allowed to travel within a small space. With the rapid propagation of the CME, as our previous works indicated (see Fig. 6*g* of Lin 2002 and Figs. 8 and 9 of Lin et al. 2004), the length of the current sheet and the volume of the disrupting magnetic field quickly increase, the room for electrons to move also quickly expands simultaneously, and the energetic electrons may eventually escape to the outermost corona and interplanetary space as they come across the open field. This scenario leads us to expect that some type III bursts (especially those that serve as precursors of the associated type II bursts) manifest a short drift range in frequency at the beginning of the eruption (e.g., see Zlotnik et al. 1998; Klassen et al. 1999; Klassen & Pohjolainen 2002), and then the frequency drifts quickly extend to a large range toward low frequency, forming the normal type III radio bursts (refer to Fig. 1 of Klassen et al. 2003 for more details). However, the cases like that shown

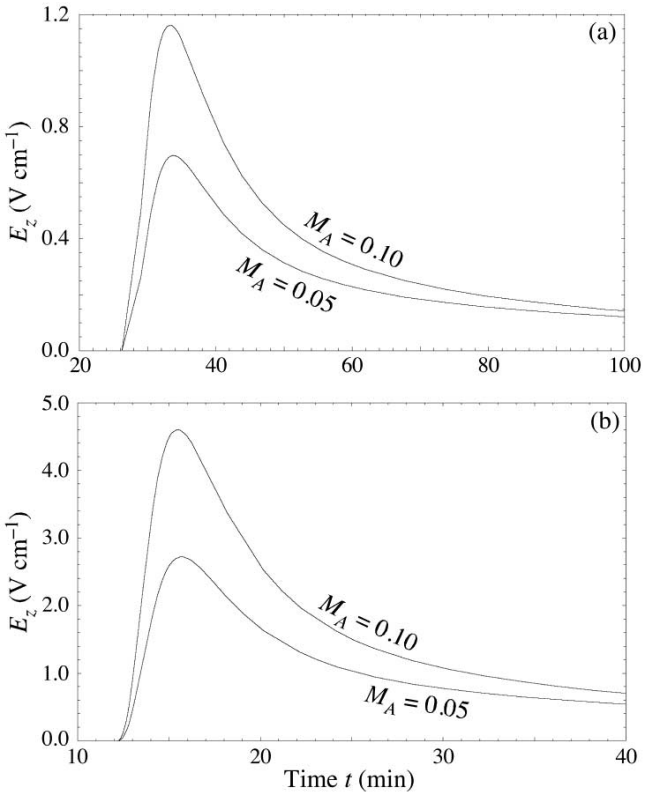

FIG. 7.—Time profiles of E_z for (*a*) $\sigma = 0.5$ and (*b*) $\sigma = 1.0$, with each panel displaying two curves that correspond to $M_A = 0.05$ and $M_A = 0.1$, respectively.

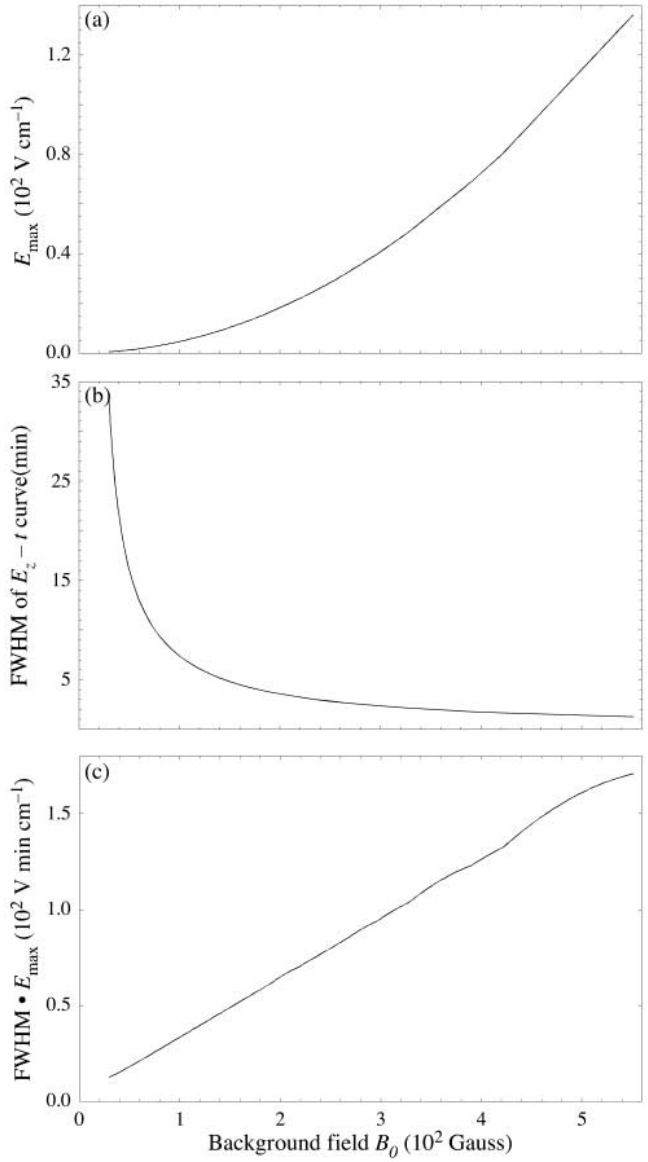

FIG. 8.—Variations of parameters for the reconnecting electric field E_z vs. σ for $M_A = 0.1$: (*a*) E_{max}, (*b*) the FWHM of the $E_z - t$ profiles, and (*c*) the product of E_{max} and the FWHM.

by Figure 6 certainly exist. In this kind of eruption, no energetic electrons escaped from the current sheet and reached the open field, and the disturbance that they caused was limited to the confined region.

Furthermore, Figure 6 and the other observations of type III radio bursts indicate that no matter how far a type III burst is able to extend to the low-frequency range, a cutoff at the high-frequency end exists for most of the type III bursts, and that the values of this cutoff frequency decrease with time in the eruption. This can be ascribed to the motion of the flare loop system in eruptions. The closed magnetic field lines holding flare loops underneath the current sheet, which are produced by magnetic reconnection, form an obstacle that prevents the energetic particles from moving in the same direction with the same energy (see Forbes & Acton 1996; Sheeley et al. 2004). The flare loop system continues to grow as a result of magnetic reconnection and forces the obstacle to move upward, causing the cutoff frequency of type III bursts to decrease. Since we mentioned earlier that our investigations of type III bursts in the present work are qualitative only, quantitative models, especially of the normal type III bursts, will be developed in the future.

4.2. *Natures of E_z and Resultant Flares*

The time t^* indicates the initiation of E_z, so it also marks the start of the flare. Figure 2 suggests the early ignition of a flare in an eruption with strong σ (see also Lin 2004). In addition to the initial time t^*, four other parameters are also important for us to be able to specify behaviors of the flare. These parameters are the maximum of the electric field, E_{max}, the time when E_z is at maximum, t_{max}, the FWHM of the time profile of E_z, and the product of the FWHM with E_{max}. Among these parameters, t_{max} has been plotted against σ in Figure 2 for easy comparison with t^*.

As we pointed out earlier, E_z directly governs the energy conversion in the eruption, so using t_{max} to approximate the time when the flare is at maximum is reasonable. The values of E_{max} determine the largest rate at which the magnetic flux is brought into the current sheet and is annihilated to heat and accelerate plasma and particles. They are approximately proportional to σ^2, as indicated by equation (12). The values of the FWHM determine the time interval in which the most efficient energy conversion process is in progress, and its product with E_{max} could be used as an index that indicates the potential impact of magnetic reconnection on heating the flare region and on accelerating charged particles. In a sense, the value of the FWHM could also describe the time interval of the flare's impulsive phase.

Figure 7 plots the time profiles of E_z for $\sigma = 0.5$ (Fig. 7*a*) and for $\sigma = 1.0$ (Fig. 7*b*), with each panel displaying two curves corresponding to $M_A = 0.05$ and $M_A = 0.1$, respectively. The two curves in each panel start at the same time, because t^* does

not depend on M_A. They differ from each other by a factor of the ratio of the two values of M_A, but they almost have the same value of t_{max} and the same FWHM. Thus, in Figures 2 and 8 we just display the variations of t_{max} and the other four parameters for $M_A = 0.1$ only. The plots in Figure 2 and each panel in Figure 8 reveal important observational consequences of solar flares and their correlations to type II radio bursts.

We note that both the t_{max} and t^* curves shown in Figure 2 suggest the early impulsive phase of the flare as the eruption takes place in a magnetic structure with large σ. This is consistent with the conclusion of Lin (2004). As indicated by equation (12), Figure 8*a* shows the quadratic dependence of E_{max} on σ. Figures 8*b* and 8*c* imply that the most violent energy conversion occurs in a short period after the triggering of the eruption, and its impact on the consequent processes increases in an apparent way with σ.

Functional behaviors of various parameters for E_z against σ, shown in Figures 2 and 8, are suggestive of the early occurrence of the particle acceleration by E_z and the very energetic particle beams produced in major eruptions. This leads us to expect that the hard X-ray emissions due to nonthermal electrons and the early type III radio burst that constitutes the precursor of the associated type II bursts will take place simultaneously in the relevant events, as observed by Klassen et al. (2003). Furthermore, correlations of type II bursts with the other manifestations could be revealed by comparing t^* and t_{max} in Figure 2 with t_{in} in Figures 4*b* and 5*b*.

We find that the lag of the type II burst behind its precursors and the associated flare is not apparent, provided that magnetic reconnection in the current sheet is fast ($M_A = 0.1$). In a typical eruptive process (usually with $\sigma > 50$ G), such a lag is within 30 minutes (either $t_{in} - t^*$ or $t_{in} - t_{max}$), and the correlation of type II bursts to solar flares, CMEs, hard X-ray emission, and type III bursts is easy to establish. The results of Mancuso et al. (2002) suggested a lag of 2.5 minutes, Klassen et al. (2003) reported a lag of about 2 minutes, and Figure 6 indicates that the onset of type II bursts in the 2003 October 26 event was 4.5 minutes behind that of the precursors. Combining these results with those that can be deduced from Figures 2 and 8*b* qualitatively replicates the conclusions given by Cane & Reames (1988), which are that type II bursts typically start at the time when the Hα flare reaches the maximum and that the start frequency of the type II burst is typically higher when the associated flare has a shorter impulsive phase.

In the case of slow reconnection ($M_A = 0.05$), on the other hand, establishing the above correlations is not trivial. In order to invoke type II bursts earlier with high frequencies at lower altitudes, the disrupting magnetic configuration should have a stronger background field ($\sigma > 1.5$; note the position of the turning point T1 in Fig. 4). For a weak background field ($\sigma < 1.5$), the CME-driven shock may never form, as we have pointed out. Even if the CME-driven shock could form at the lower altitudes, it might also disappear at higher altitudes (note the shape of the curves between the two turning points T1 and T2) unless the background field was very strong ($\sigma > 4$). In the case of $\sigma = 1.4$ and $M_A = 0.05$, we have $t^* = 8.6$ minutes, and t_{max} is about 10 minutes, which is roughly the same as that for $M_A = 0.1$. But Figure 4*b* shows that the onset of a type II burst could be as late as $t_{in} = 50$ minutes, and the onset position might be as high as 10 $R_\odot$. With such a large difference between onset times of various manifestations, it is very hard to establish any correlation among them, since the other eruptions are quite likely to occur during this period, especially during the solar maximum. Another issue that makes the job even harder is that the CME-driven shock, and thus the type II burst, might not be ignited at all. This result, combined with those from $M_A = 0.1$, implies from a different viewpoint that the role of magnetic reconnection in governing CME propagations and the resultant type II radio bursts is more significant than that of the strength of the magnetic field.

5. CONCLUSIONS

After modifying our previous works related to the catastrophe model of solar eruptions, we have investigated the behaviors of the electric field induced by magnetic reconnection inside the current sheet, the CME propagations, and the onset positions and times of radio bursts of types II and III during the eruption. Modifications were made by including the impact of gravity of the prominence material inside the flux rope and the excess mass brought into the CME bubble by magnetic reconnection through the current sheet on the catastrophe and on the CME propagation. According to the works of Lin et al. (2004) and Lin & Soon (2004), we paid the necessary attention to various components of CME velocities that can be obtained from observations and distinguished the one that may account for the ignition of the CME-driven shocks from the others. This helps us determine the onset positions, times, and start frequencies of the type II radio burst. Consequent implications of our results to observations were carefully analyzed and discussed. The main results are summarized as follows.

1. Because of its ideal MHD nature, the catastrophic behavior of the disrupting magnetic field is not affected by the excess of the material that results from magnetic reconnection. The impact of gravity on the catastrophe occurring in the magnetic configuration including a flux rope with 2.1×10^{16} g of material becomes apparent when the average strength of the background field on the boundary surface B_0 is weaker than 30 G (or $\sigma < 0.3$; see also Isenberg et al. 1993 and Lin 2004). But the impact of the added mass does affect the CME propagation. For a flux rope with the same initial mass, the added material causes the CME propagation to suffer from deceleration as $\sigma < 0.685$ for $M_A = 0.05$, or as $\sigma < 0.423$ for $M_A = 0.1$. As the value of σ exceeds these thresholds, on the other hand, the impact of gravity becomes dim.

2. Both σ and M_A play an important role in governing the onset and the subsequent evolutionary features of type II radio bursts. With a strong magnetic field and fast reconnection, the velocity at the CME's leading edge may quickly exceed the local Alfvén speed and invoke type II bursts at low altitudes and with high start frequencies. For the major eruption that develops into a CME with a terminal speed of around 1000 km s^{-1} (with $\sigma > 0.7$ and $M_A = 0.1$, or with $\sigma > 1.5$ and $M_A = 0.05$), we estimated that the onset position of type II bursts is at around 0.5 $R_\odot$, corresponding to the start frequency of the fundamental lane of 150 MHz. B. Vršnak (2006, private communication) suggested that a value of 150 MHz might be too large for an altitude of 0.5 $R_\odot$ and that 110 MHz seems more appropriate.

3. In governing the onset positions, times, and start frequencies of type II radio bursts, the roles of M_A and σ roughly compensate each other (refer to Figs. 4 and 5); namely, for $M_A\sigma =$ constant, values of these parameters for the type II bursts are roughly the same. But the positions of the two turning points and the shapes of those curves shown in Figures 4 and 5 indicate that the other properties of type II bursts are more dependent on M_A than on σ. The functional behavior of the Alfvén speed

versus the altitude determines that even fast CMEs (>800 km s^{-1}) may not be able to produce type II bursts if M_A is small. Examples of the radio-quiet fast CMEs have been reported by many authors (e.g., see Gopalswamy 2004b, pp. 223–224).

4. The precursor of type II bursts consists of a sequence of type III bursts that are produced by electron beams accelerated by the electric field E_z in the reconnecting current sheet at the early stage of the eruption. The motions of these electrons are confined in the current sheet, which is short at the beginning, so the frequency drift range of the precursor on the dynamic spectrum is small and may evolve to the ordinary type III bursts as the current sheet becomes long enough or as electron beams meet the open fields.

5. Because E_z governs the absolute rate of energy conversion via magnetic reconnection, its evolutionary behaviors may be used to determine some features of solar flares, such as the initial and maximum times. Both the times are very close to the onset time of the eruption for the background field with intermediate strength ($\sigma \geq 0.5$), which implies that the flare is well associated with the CME in the relevant eruptive process. But it is not easy to build up the association of type II bursts with flares if the coronal environment does not allow fast reconnection to occur unless the background field is fairly strong ($\sigma \geq 1.5$; compare Fig. 4 with Fig. 8).

6. Overall, our studies of the type II radio burst in the present work are based on the assumption that the type II burst is caused by the CME-driven shock. But the cause of the type II burst, especially the metric type II burst, is still an open question. Recent works by Cane & Erickson (2005), Pohjolainen & Lehtinen (2006), and Vršnak et al. (2006) investigated various eruptive events and noted that the CME might not be the driver of the shocks that ignite the type II bursts, although problems exist with the assumption that those shocks are not being driven by CMEs.

The authors are grateful to H. V. Cane, P. Chen, J. C. Raymond, L. Sui, and B. Vršnak for valuable comments and suggestions. J. L.'s work at the Yunnan Astronomical Observatory (YNAO) was supported by the Ministry of Science and Technology of China under the 973 program grant 2006CB806303 to YNAO, and his work at the Center for Astrophysics was supported by NASA under grants NNG05GG38G and NAG5-12827 to the Smithsonian Astrophysical Observatory. The Hiraiso Radio Spectrograph is operated by the Communications Research Laboratory, Japan.

APPENDIX

EXPRESSIONS FOR SEVERAL VARIABLES

The expressions for some parameters in equations (2)–(4) were not given explicitly in the text. To make those equations much more understandable, we collect the expressions from Lin & Forbes (2000) and list them below:

$$
\begin{aligned}
p' &= \frac{\tilde{A}_{0h}A_{Rq} - A_{Rh}A_{0q}}{A_{Rp}A_{0q} - A_{0p}A_{Rq}},\\
q' &= \frac{A_{Rh}A_{0p} - \tilde{A}_{0h}A_{Rp}}{A_{Rp}A_{0q} - A_{0p}A_{Rq}},\\
\dot{h}' &= \left(\frac{I_0}{c}\right)^2 \frac{\lambda^2}{2mh\dot{h}L_{PQ}^2}\left[\frac{H_{PQ}^2}{2h^2} - \frac{(\lambda^2+p^2)(h^2-q^2)+(\lambda^2+q^2)(h^2-p^2)}{\lambda^2+h^2}\right],
\end{aligned}
\tag{A1}
$$

with

$$
\begin{aligned}
\tilde{A}_{0h} &= -\frac{c^2E_z}{2I_0\dot{h}} - A_{0h}\\
&= \frac{c}{2I_0}\frac{M_A B_y^2(0,y_0)}{\dot{h}\sqrt{4\pi\rho(y)}} - A_{0h},
\end{aligned}
$$

where

$$
\begin{aligned}
A_{0p} &= \frac{\lambda p(h^2+\lambda^2)(\lambda^2+q^2)}{h^2q\left[(\lambda^2+p^2)(\lambda^2+q^2)\right]^{3/2}}\left[(h^2-q^2)\Pi\left(\frac{p^2}{h^2},\frac{p}{q}\right) - h^2K\left(\frac{p}{q}\right)\right],\\
A_{0q} &= \frac{\lambda(h^2+\lambda^2)(\lambda^2+p^2)}{h^2\left[(\lambda^2+p^2)(\lambda^2+q^2)\right]^{3/2}}\left[(h^2-q^2)\Pi\left(\frac{p^2}{h^2},\frac{p}{q}\right) - h^2K\left(\frac{p}{q}\right)\right],\\
A_{0h} &= -\frac{\lambda}{h^3q\sqrt{(\lambda^2+p^2)(\lambda^2+q^2)}}\left[h^2q^2E\left(\frac{p}{q}\right) - h^2(h^2+q^2)K\left(\frac{p}{q}\right)\right.\\
&\quad \left. + (h^4-p^2q^2)\Pi\left(\frac{p^2}{h^2},\frac{p}{q}\right)\right]
\end{aligned}
\tag{A2}
$$

and

$$A_{Rp} = \frac{\lambda p\left(h^2+\lambda^2\right)}{q\left(\lambda^2+p^2\right)}\sqrt{\frac{\lambda^2+p^2}{\lambda^2+q^2}}\left\langle\left(1-\frac{p^2}{h^2}\right)\Pi\left[\sin^{-1}\left(\frac{q}{h}\right),\frac{p^2}{h^2},\frac{p}{q}\right]\right.$$
$$\left. - F\left[\sin^{-1}\left(\frac{q}{h}\right),\frac{p}{q}\right] - \frac{q}{2h}\sqrt{\frac{h^2-q^2}{h^2-p^2}}\left\{1+\ln\left[\frac{\lambda H_{PQ}^3}{r_{00}L_{PQ}(h^4-p^2q^2)}\right]\right\}\right\rangle,$$

$$A_{Rq} = \frac{\lambda\left(h^2+\lambda^2\right)}{\left(\lambda^2+q^2\right)}\sqrt{\frac{\lambda^2+q^2}{\lambda^2+p^2}}\left\langle\left(1-\frac{p^2}{h^2}\right)\Pi\left[\sin^{-1}\left(\frac{q}{h}\right),\frac{p^2}{h^2},\frac{p}{q}\right]\right.$$
$$\left. - F\left[\sin^{-1}\left(\frac{q}{h}\right),\frac{p}{q}\right] - \frac{q}{2h}\sqrt{\frac{h^2-p^2}{h^2-q^2}}\left\{1+\ln\left[\frac{\lambda H_{PQ}^3}{r_{00}L_{PQ}(h^4-p^2q^2)}\right]\right\}\right\rangle,$$

$$A_{Rh} = \frac{\lambda}{2h^2L_{PQ}H_{PQ}}\left\{\frac{2h^6-2(\lambda pq)^2}{h^2-\lambda^2} - \frac{h^2\left(p^2+q^2\right)\left(h^2-\lambda^2\right)}{h^2-\lambda^2}\right.$$
$$\left. + \left(h^4-p^2q^2\right)\ln\left[\frac{\lambda H_{PQ}^3}{r_{00}L_{PQ}(h^4-p^2q^2)}\right]\right\}$$
$$+\frac{\lambda}{hqL_{PQ}}\left\{\left(h^2+q^2\right)F\left[\sin^{-1}\left(\frac{q}{h}\right),\frac{p}{q}\right] - q^2E\left[\sin^{-1}\left(\frac{q}{h}\right),\frac{p}{q}\right]\right.$$
$$\left. - \left(h^2-\frac{p^2q^2}{h^2}\right)\Pi\left[\sin^{-1}\left(\frac{q}{h}\right),\frac{p^2}{h^2},\frac{p}{q}\right]\right\}. \quad \text{(A3)}$$

Here K, E, and Π in equations (A2) are the first, second, and third kinds of complete elliptic integrals, respectively, F, E, and Π in equations (A3) are the first, second, and third kinds of incomplete elliptic integrals, respectively, and B_y in the expression for $\tilde{A}_{0h}$ can be deduced from equation (9).

REFERENCES

Akmal, A., Raymond, J. C., Vourlidas, A., Thompson, B. J., Ciaravella, A., Ko, Y.-K., Uzzo, M., & Wu, R. 2001, ApJ, 553, 922
Aly, J. J. 1984, ApJ, 283, 349
———. 1991, ApJ, 375, L61
Cane, H. V., & Erickson, W. C. 2005, ApJ, 623, 1180
Cane, H. V., Erickson, W. C., & Prestage, N. P. 2002, J. Geophys. Res., 107, 1315
Cane, H. V., & Reames, D. V. 1988, ApJ, 325, 895
Ciaravella, A., Raymond, J. C., Reale, F., Strachan, L., & Peres, G. 2001, ApJ, 557, 351
Dulk, G. A., LeBlanc, Y., Bastian, T. S., & Bougeret, J.-L. 2000, J. Geophys. Res., 105, 27343
Emslie, A. G., et al. 2004, J. Geophys. Res., 109, A10104
Filippov, B., & Koutchmy, S. 2002, Sol. Phys., 208, 283
Forbes, T. G. 2000, J. Geophys. Res., 105, 23153
———. 2003, Adv. Space Res., 32, 1043
Forbes, T. G., & Acton, L. W. 1996, ApJ, 459, 330
Forbes, T. G., & Isenberg, P. A. 1991, ApJ, 373, 294
Forbes, T. G., & Lin, J. 2000, J. Atmos. Sol.-Terr. Phys., 62, 1499
Forbes, T. G., & Malherbe, J. M. 1991, Sol. Phys., 135, 361
Gary, D. E., Dulk, G. A., House, L., Illing, R., Sawyer, C., Wagner, W. J., McLean, D. J., & Hildner, E. 1984, A&A, 134, 222
Gopalswamy, N. 2004a, in Solar and Space Weather Radiophysics: Current Status and Future Developments, ed. D. E. Gary & C. U. Keller (Dordrecht: Kluwer), 305
———. 2004b, in The Sun and The Heliosphere as an Integrated System, ed. G. Poletto & S. T. Suess (Dordrecht: Kluwer), 201
Gopalswamy, N., Lara, A., Kaiser, M. L., & Bougeret, J.-L. 2001a, J. Geophys. Res., 106, 25261
Gopalswamy, N., Yashiro, S., Kaiser, M. L., Howard, R. A., & Bougeret, J.-L. 2001b, J. Geophys. Res., 106, 29219
Howard, R. A., Brueckner, G. E., St. Cyr, O. C., & Biesecker, D. A. 1997, in Coronal Mass Ejections, ed. N. Crooker, J. A. Joselyn, & J. Feynman (Washington, DC: AGU), 17
Howard, R. A., Sheeley, N. R., Jr., Koomen, M. J., & Michels, D. J. 1985, J. Geophys. Res., 90, 8173
Isenberg, P. A., Forbes, T. G., & Démoulin, P. 1993, ApJ, 417, 368
Ji, H., Wang, H., Schmahl, E. J., Moon, Y.-J., & Jiang, Y. 2003, ApJ, 595, L135
Jing, J., Qiu, J., Lin, J., Qu, M., Xu, Y., & Wang, H. 2005, ApJ, 620, 1085
Klassen, A., Aurass, H., Klein, K.-L., Hofmann, A., & Mann, G. 1999, A&A, 343, 287
Klassen, A., Aurass, H., Mann, G., & Thompson, B. J. 2000, A&AS, 141, 357
Klassen, A., & Pohjolainen, S. 2002, in Solar Variability: From Core to Outer Frontiers, ed. A. Wilson (ESA-SP 506; Noordwijk: ESA), 307
Klassen, A., Pohjolainen, S., & Klein, K.-L. 2003, Sol. Phys., 218, 197
Klimchuk, J. A. 2001, in Space Weather, ed. P. Song, H. J. Singer, & G. Siscoe (Washington, DC: AGU), 143
Ko, Y., Raymond, J. C., Lin, J., Lawrence, G., Li, J., & Fludra, A. 2003, ApJ, 594, 1068
Kondo, T., Isobe, T., Igi, S., Watari, S., & Tokumaru, M. 1995, J. Commun. Res. Lab., 42, 111
Kundu, M. R. 1965, Solar Radio Astronomy (New York: Wiley)
Lee, M. A. 2005, ApJS, 158, 38
Lin, J. 2001, Ph.D. thesis, Univ. New Hampshire
———. 2002, Chinese J. Astron. Astrophys., 2, 539
———. 2004, Sol. Phys., 219, 169
Lin, J., & Forbes, T. G. 2000, J. Geophys. Res., 105, 2375
Lin, J., Forbes, T. G., Priest, E. R., & Bungey, T. N. 1995, Sol. Phys., 159, 275
Lin, J., Ko, Y.-K., Sui, L., Raymond, J. C., Stenborg, G. A., Jiang, Y., Zhao, S., & Mancuso, S. 2005, ApJ, 622, 1251
Lin, J., Raymond, J. C., & van Ballegooijen, A. A. 2004, ApJ, 602, 422
Lin, J., & Soon, W. 2004, NewA, 9, 611
Lin, J., Soon, W., & Baliunas, S. L. 2003, NewA Rev., 47, 53
Litvinenko, Y. E. 1996, ApJ, 462, 997
———. 2003, Sol. Phys., 212, 379
Mancuso, S., & Raymond, J. C. 2004, A&A, 413, 363
Mancuso, S., Raymond, J. C., Kohl, J. L., Ko, Y.-K., Uzzo, M., & Wu, R. 2002, A&A, 383, 267
Mann, G., Klassen, A., Aurass, H., & Classen, H.-T. 2003, A&A, 400, 329
Miyagoshi, T., & Yokoyama, T. 2004, ApJ, 614, 1042
Pick, M., Démoulin, P., Krucker, S., Malandraki, O., & Maia, D. 2005a, ApJ, 625, 1019
Pick, M., Malherbe, J.-M., Kerdraon, A., & Maia, D. J. F. 2005b, ApJ, 631, L97
Pohjolainen, S., & Lehtinen, N. J. 2006, A&A, 449, 359
Priest, E. R. 1982, Solar Magneto-hydrodynamics (Dordrecht: Reidel)
Priest, E. R., & Forbes, T. G. 2002, A&A Rev., 10, 313
Qiu, J., Wang, H., Cheng, C. Z., & Gary, D. E. 2004, ApJ, 604, 900

Raymond, J. C., et al. 2000, Geophys. Res. Lett., 27, 1439
Reeves, K. K., & Forbes, T. G. 2005, ApJ, 630, 1133
Schmieder, B., Forbes, T. G., Malherbe, J. M., & Machado, M. E. 1987, ApJ, 317, 956
Sheeley, N. R., Jr., Warren, H. P., & Wang, Y.-M. 2004, ApJ, 616, 1224
Sittler, E. C., Jr., & Guhathakurta, M. 1999, ApJ, 523, 812
Sturrock, P. A. 1991, ApJ, 380, 655
Sui, L., Holman, G. D., White, S. M., & Zhang, J. 2005, ApJ, 633, 1175
Švestka, Z. 1976, Solar Flares (Dordrecht: Reidel)
———. 1996, Sol. Phys., 169, 403
Vourlidas, A. 2004, in Solar and Space Weather Radiophysics: Current Status and Future Developments, ed. D. E. Gary & C. U. Keller (Dordrecht: Kluwer), 223
Vršnak, B., Warmuth, A., Temmer, M., Veronig, A., Magdalenić, J., Hillaris, A., & Karlický, M. 2006, A&A, 448, 739
Wagner, W. J. 1982, Adv. Space Res., 2, 203
Wagner, W. J., & MacQueen, R. M. 1983, A&A, 120, 136
Wood, P., & Neukirch, T. 2005, Sol. Phys., 226, 73
Yokoyama, T., Akita, K., Morimoto, T., Inoue, K., & Newmark, J. 2001, ApJ, 546, L69
Yokoyama, T., & Shibata, K. 1994, ApJ, 436, L197
Zlotnik, E. Y., Klassen, A., Klein, K.-L., Aurass, H., & Mann, G. 1998, A&A, 331, 1087